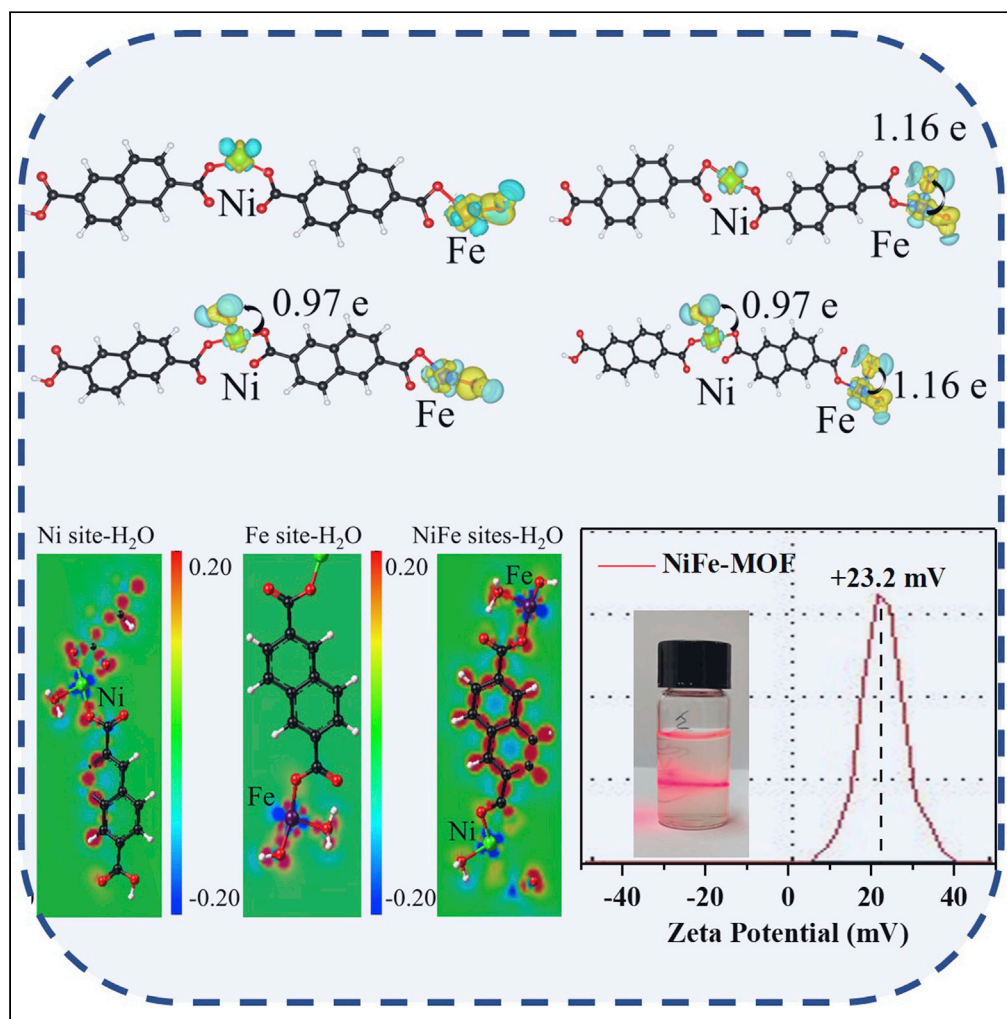


Article

Bioinspired inhibition of aggregation in metal-organic frameworks (MOFs)



Licheng Yu,
Zhihao Nie,
Sicong Xie, ...,
Jingjing Duan,
Markus Antonietti,
Sheng Chen

chicheng@unimelb.edu.au
(C.C.)
jingjing.duan@njust.edu.cn
(J.D.)
sheng.chen@njust.edu.cn
(S.C.)

Highlights

A study of fabricating
MOF colloids was
proposed by using water
as a "stabilizer"

The results challenge a
common concept that
MOFs are non-solution-
processable

DFT calculations show
electrostatic repulsion
mechanism to stabilize
MOF dispersion

NiFe-MOF dispersions
can be separated to
produce MOF with
different size

Article

Bioinspired inhibition of aggregation in metal-organic frameworks (MOFs)

Licheng Yu,¹ Zhihao Nie,¹ Sicong Xie,¹ Lili Jiang,¹ Baokai Xia,¹ Ming Li,¹ Chi Cheng,^{1,*} Jingjing Duan,^{1,*} Markus Antonietti,² and Sheng Chen^{1,3,4,*}

SUMMARY

Different from traditional procedures of using solid stabilizers like polymers and surfactants, here we demonstrate that water, as a very “soft” matter, could function as a “spacer” to prevent the aggregation of metal-organic frameworks (MOFs) in aqueous dispersions. Our theoretical calculations reveal in case of an excess of positively charged metal nodes of MOFs, where water molecules are ligated to metal nodes that greatly enhance MOFs’ solution dispersibility through electrostatic stabilization. This discovery has motivated us to develop a facile experimental approach for producing a category of “clean” MOF dispersions without foreign additives. Potential application has been demonstrated for the size fractionation of MOFs, which results in small-size MOFs (50–80 nm) characteristic of superior electrocatalytic oxygen evolution activities (256 mV at 10 mA cm⁻², Tafel slope of 49 mV dec⁻¹ and durability >30 h). This work would provide new clues for aqueous processing of MOFs for many emerging applications.

INTRODUCTION

Metal-organic framework (MOF) is an emerging category of porous materials that have received enormous interests recently.^{1–4} This kind of functional materials is desirable for promising utilizations in technological areas such as catalysis and separation.^{5–9} Nevertheless, a lack of an effective strategy to fabricate processable MOFs in large quantities has become a significant obstacle to exploiting most proposed applications.^{10–13}

Like many other materials,^{14–17} one of the challenging problems in the fabrication of stable MOF dispersions is aggregation. MOFs have intrinsically high surface areas, which unless well separated, tends to aggregate for minimizing surface energies. Recent efforts aimed at inhibiting aggregation has been devoted to decorating MOFs with foreign stabilizers such as guest functional groups,^{18–20} polymers,²¹ and nanocapsule.^{19,21,22} But these “solid” stabilizers are detrimental for most applications.^{23–39} New procedures to fabricate “clean” MOF dispersions are highly desirable.

In nature, it is observed that many colloids (like egg-white and blood) have formed without the need of foreign stabilizers. The key chemistry component for forming these dispersions is electric double layers (quantified by zeta potentials), which could promote the stabilization thorough electrostatic repulsion. Motivated by this interesting phenomenon, here we report a facile procedure to produce MOF dispersions. The critical step is to manipulate the ratios of metal precursor/organic ligand in synthetic process. As an example, NiFe-MOF synthesized with the molar ratios of Ni²⁺/Fe²⁺/organic ligands of 6.5/1.0/6.7 that allows for forming stable dispersions characteristic of positive surface charges (up to Zeta potential of +29.7 mV). This has led to a class of “clean” MOF dispersions without involving foreign additives. Potential utilizations have been further demonstrated for separating MOFs according to their lateral size, where the as-resultant small-size MOFs have shown excellent electrocatalytic activities.

At present, many catalytic materials for OER have been fabricated (especially metal Ni, Co, and Fe), for example, NiCo-LDH/RuO₂⁴⁰ that demonstrated an overpotential of 276 mV at current density of 10 mA cm⁻² and a Tafel slope of 79.4 mV dec⁻¹, NiFe LDH⁴¹ showing an overpotential of 302 mV and a Tafel slope of 40 mV dec⁻¹ and NiFe LDHs VFe⁴² showing an overpotential of 245 mV and a Tafel slope of 70 mV dec⁻¹, etc. In this paper, we first synthesized ultrathin two-dimensional NiFe-MOF nanosheets. Through simple electrostatic repulsion separation, we obtained ultrathin MOF nanosheets with more uniform size and

¹Key Laboratory for Soft Chemistry and Functional Materials (Ministry of Education), School of Chemistry and Chemical Engineering, School of Energy and Power Engineering, Nanjing University of Science and Technology, Nanjing 210094, China

²Department of Chemical Engineering, University of Melbourne, Parkville, VIC, Australia

³Max Planck Institute of Colloids and Interfaces, 14476 Potsdam, Germany

⁴Lead contact

*Correspondence: chicheng@unimelb.edu.au (C.C.), jingjing.duan@njust.edu.cn (J.D.), sheng.chen@njust.edu.cn (S.C.)

<https://doi.org/10.1016/j.isci.2023.106239>



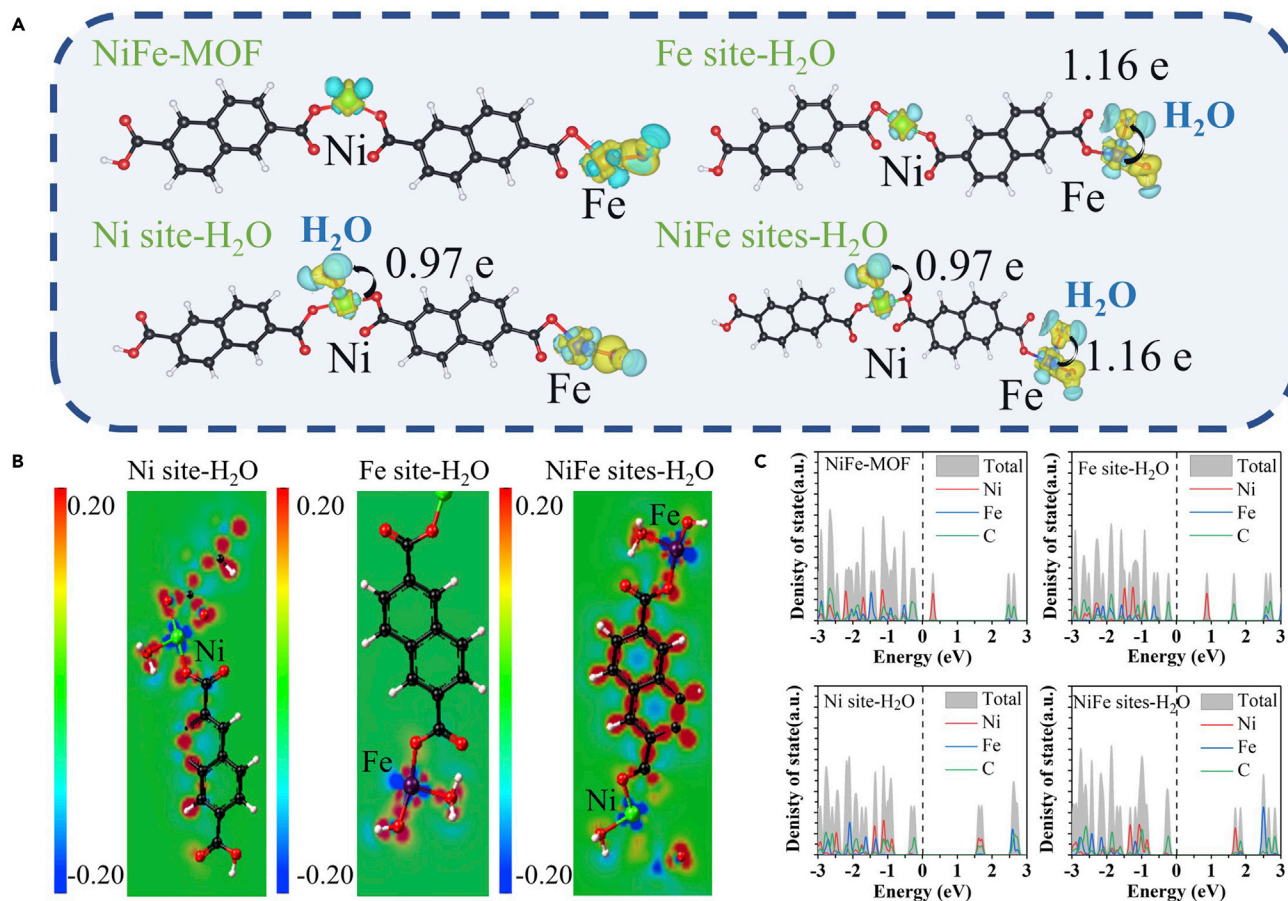


Figure 1. DFT calculations of NiFe-MOF interacted with H₂O via electro-static induction

(A) Schematic 3D images of charge density difference of NiFe-MOF, Fe site-H₂O, Ni site-H₂O and NiFe sites-H₂O. The yellow isosurface ($7.5 \times 10^{-3} \text{ e}/\text{\AA}^3$) represents electron accumulation and the blue isosurface ($7.5 \times 10^{-3} \text{ e}/\text{\AA}^3$) represents electron depletion.

(B) Schematic 2D slice of charge density difference of NiFe-MOF absorbs H₂O with different metal site, while blue represents the electron accumulation while red means the electron depletion area. Ni site-H₂O, Ni atom adsorbs one H₂O molecule. Fe site-H₂O, Ni atom adsorbs one H₂O molecule and NiFe sites-H₂O, both Fe and Ni atoms adsorb one H₂O molecule, respectively. Black spheres represent C atoms. Red spheres represent O atom. White spheres represent H atoms. Green spheres and blue spheres represent Ni and Fe atoms.

(C) Density of state of NiFe-MOF with and without adsorbed H₂O atom. DOS of NiFe-MOF, Ni site-H₂O, Fe site-H₂O and NiFe sites-H₂O.

smaller transverse dimension, which showed good performance of over potential of 256 mV, Tafel slope of 49 mV dec^{-1} and stability of more than 30 h at a current density of 10 mA cm^{-2} .

RESULTS

The theoretical structural model of NiFe-MOF is defined as follows: metal ions ($M = \text{Ni, Fe}$) exist in the form of $[\text{MO}_6]$ octahedral units; two $[\text{MO}_6]$ units are coordinated with two *trans* monodentate carboxylates. In addition, we have built the structural model of H₂O ligated onto different metal sites (Ni, Fe, Ni & Fe) of MOFs, which is used to simulate the behavior of MOF in aqueous solutions.^{26,27} Figure 1A demonstrates both the original structures and corresponding schematic 3D images of charge density difference. As compared to pristine NiFe-MOF, there are obvious electron accumulation regions between O atoms and metal atoms after ligated with H₂O molecules, which signifying the positive charge transfers from MOFs to H₂O. This result is consistent with the Bader charge analysis, which shows the Ni and Fe sites are slightly more positive (0.97 e and 1.16 e) after ligated with H₂O molecules as compared to pristine NiFe-MOF (0.90 e and 1.15 e), indicating that the positive surface charges of NiFe-MOF also transfer into water molecules in the aqueous solution.

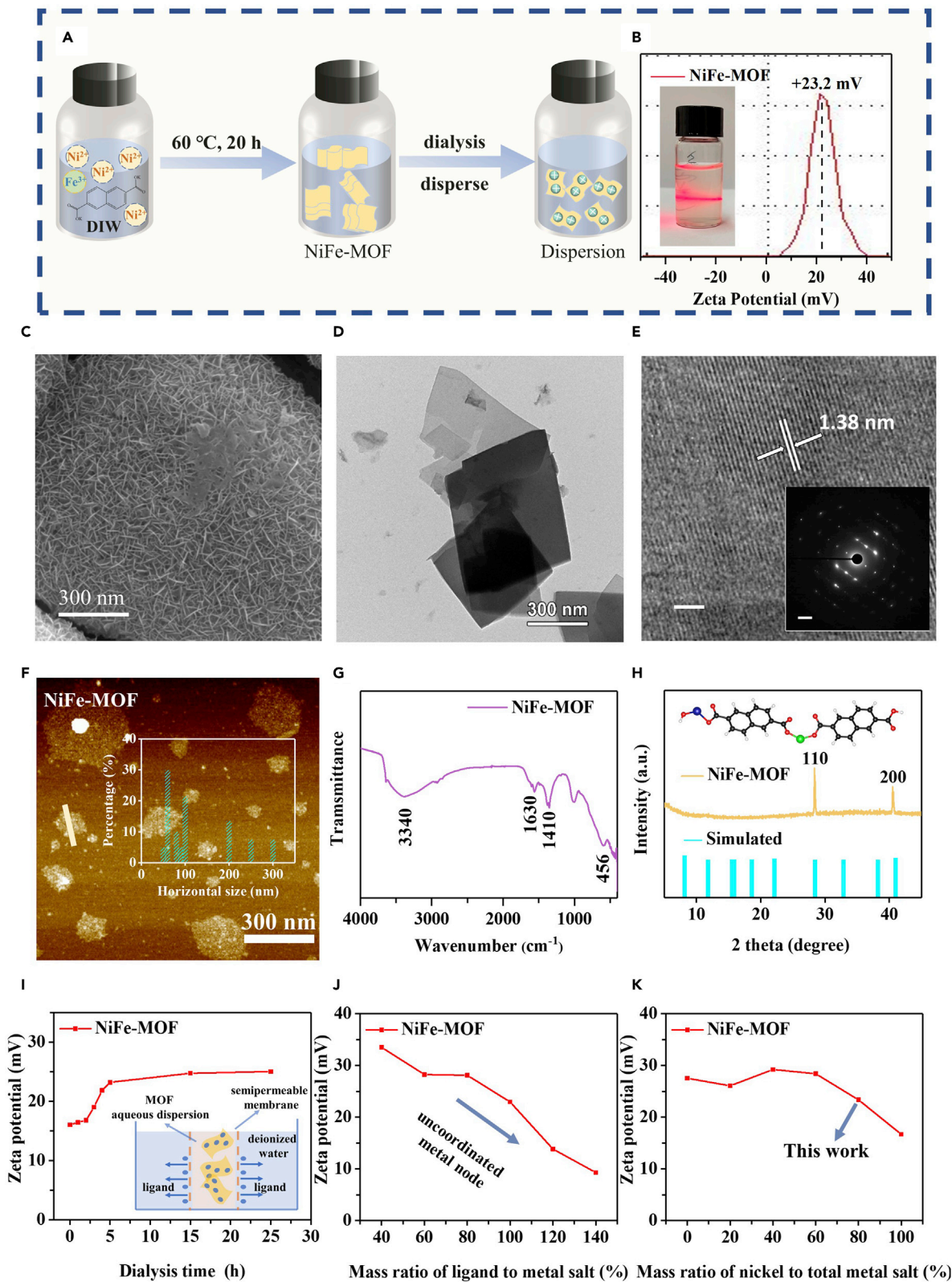


Figure 2. Preparation and morphological characterizations of NiFe-MOF dispersed in water

- (A) Schematic illustration of synthesizing NiFe-MOF aqueous dispersions.
 (B) The zeta potential of NiFe-MOF aqueous solution. The inset is a photograph of NiFe-MOF aqueous solution with Tyndall effect.
 (C) Scanning electron microscopy (SEM) images.
 (D) Transmission electron microscopy (TEM) image.
 (E) High-resolution transmission electron microscopy (HRTEM) image (scale bar: 5 nm) and selected area electron diffraction (SAED) pattern (scale bar, 2/1 nm).
 (F) Atomic force microscopy (AFM) image and corresponding height profile along the marked green line.
 (G) Fourier Transform Infrared Spectrometer (FTIR) spectra of NiFe-MOF.
 (H) XRD patterns of NiFe-MOF and simulated Ni-MOF, which suggests the 2 theta degrees of all the diffraction peaks are close to that of $\text{Ni}(\text{C}_{12}\text{H}_6\text{O}_4)(\text{H}_2\text{O})_4$, the inset is the 2D framework structure of NiFe-MOF.
 (I) Zeta potentials of NiFe-MOF aqueous dispersion change with dialysis time, and the insert is the schematic diagram of the dialysis process.
 (J) Zeta potentials of NiFe-MOF aqueous dispersion change with the mass ratios of ligands/metal salts (the mass ratio of nickel and iron were fixed as 4:1).
 (K) Zeta potentials of NiFe-MOF aqueous dispersion with the mass ratios of nickel to total metal salts (the mass ratio of metal salts/ligand were fixed as 1:1).

To better understand the charge transfer process, the corresponding in-silico structures have been further examined. As shown in Figure 1B, the schematic 2D slice of the charge density difference of NiFe-MOF clearly demonstrate the expected positive partial charge at Ni and Fe and the partially compensating negative charge at the oxygen side. Notably, when a H_2O molecule is ligated onto NiFe-MOF, there is obvious charge re-distribution inside the whole structures, bringing positive polarization into the continuous water structure. The strong interactions between metal sites and H_2O are verified by structural and energy analyses in Table S1, where the structure of NiFe-MOF with both metal sites ligated with H_2O molecules show the shortest bond lengths of Ni-O and Fe-O (1.963 Å and 1.935 Å) and optimal adsorption energy (−2.939 eV) as compared to other cases. Further, the strong ligand effect has been revealed by DOS shown in Figure 1C, where the Femi levels of metal sites shift positive after adsorption of H_2O molecules. Based on above theoretical calculations, it can be hypothesized that in the case of an excess of metal nodes (i.e., MOFs' surface terminated by cations), MOFs are ligated with H_2O molecules to that can form stable MOFs colloids thorough electrostatic repulsion.

Experimentally, the NiFe-MOF has been synthesized by a hydrothermal method by using nickel acetate and iron nitrates as metal precursors and naphthalene dicarboxylic acid dipotassium as organic ligand precursor (Figure 2A).²⁸ We have noted that the key step for making stable MOF colloids is to manipulate the ratios between metal salts and organic ligands. Next, the pristine sample was subjected to dialysis in water for 12 h, where weakly bound bridging units are removed, leaving cation terminated crystal surface planes with NO_3^- as counterions. The resultant colloidal product was collected by centrifugation and re-dispersed in water with a concentration of $\sim 0.2 \text{ mg mL}^{-1}$.

The morphology of as-synthesized NiFe-MOF was characterized by scanning electron microscopy (SEM) as ultrathin nanosheets (Figure 2C). The lateral and vertical dimensions of NiFe-MOF are imaged by transmission electron microscopy (TEM) and atomic force microscopy (AFM, Figure 2F), which show mixed-size nanosheets in the range of tens to hundreds of nanometers (Figure 2D) with an average thickness of 1.5–2.4 nm. Notably, these NiFe-MOF nanosheets have good crystalline structures as revealed by the clear lattice fringe lattice spacing of $\sim 1.4 \text{ nm}$ (due to the slit-like pores formed between adjacent metal-organic carbon layers, Figure 2E), in addition to well-defined peaks (corresponding to 110 and 200 crystal faces, respectively) in X-ray diffraction (XRD, Figure 2H) profiles,²⁹ as the XRD simulation results are based on bulk MOF, while the NiFe-MOF prepared in this paper was ultrathin nanosheets (thickness of 1.5–2.4 nm). The size effect leads to different crystal surface exposure, and part of the diffraction peaks disappear.

As expected, the as-obtained NiFe-MOF can form stable colloidal dispersions, exhibiting obvious Tyndall effect without aggregation even after several days (Figure 2B). Particularly, control experiments have been conducted to examine the influence of different synthetic parameters. Firstly, NiFe-MOF dispersions were obtained at different dialysis durations, during which the weak bridging ligands on the surface of MOFs were gradually removed, and consequently the NiFe-MOF has shown more positive charges from 0 to 5 h, and reached a stable value after dialysis for about 5 h (Figure 2I). Secondly, we only adjust the mass ratio of ligands/metal salts while keeping all the other parameter's constant. With the increase of the mass ratios from 0 to 1.4, the zeta potential values of as-synthesized NiFe-MOF aqueous dispersion gradually decreased (Figure 2J), indicating more metal nodes have been coordinated with organic ligands. Further, the mass ratios of Ni and Fe have been examined while keeping the other parameters fixed. As

shown in Figure 2K, it can be clearly seen that the zeta potentials have slightly dropped and then increased to its maximum value of +29.7 mV at the mass ratios of 40%. When the Ni content exceeds 40%, and the zeta potential values of the formed MOF aqueous dispersion sharply decreases. This result indicates stronger coordination capability of Ni than Fe to the organic ligands. In this paper, the excessive metal node was speculated to adjust the positive charge on the surface of MOF colloid, and dialysis can effectively remove the weak binding ligand adsorbed on the MOF surface through electrostatic attraction, and thus could improve the accuracy of subsequent experiments. The experimental results show that the zeta potential of the obtained MOF dispersion drops sharply, indicating that the number of positive metal nodes decreases significantly. Finally, the proportion of Fe/Ni in the metal was explored, and it was found that the effect was not significant, and the regulated metal salt and organic ligand was the key step. The temperature and salt concentration control experiments (Figures S5 and S6) in the hydrothermal reaction process were supplemented. It can be seen from the results that temperature and salt concentration have little influence on zeta potentials of MOF dispersions. All the above results are consistent to previous hypothesis, highlighting the importance of excess metal nodes for manipulating the surface charges of MOFs.

The structure of NiFe-MOF was further characterized by Fourier transform infrared spectrometer (FT-IR, Figure 2G) that shows characteristic peaks in the range from 1000 to 2000 cm^{-1} originated from organic ligands of MOF backbones.²⁹ In addition, X-ray photoelectron spectroscopy (XPS, Figures 3C–3F) reveals the material composed of Ni, Fe, O, and C as the main components (Figures 3C–3F), and the Fe/Ni mass ratio is 1:7.6 detected by ICP test (Table S3), and thus determines the chemical formula of NiFe-MOF as $\text{Ni}_{0.9}\text{Fe}_{0.1}(\text{C}_{12}\text{H}_6\text{O}_4)(\text{H}_2\text{O})_4$.^{29,36} Importantly, the XPS Ni $2p_{3/2}$ peak located at 856 eV indicates the oxidation state of +2 for Ni, while XPS Fe $2p_{1/2}$ at 723 eV reflects an oxidation state of +2 for Fe inside MOF structure. This result is consistent with the evidence of X-ray absorption near-edge spectroscopy (XANES, Figures 3A and 3B), in which the signal data of elemental Fe and FeO were also provided. The height of the curve indicates their valence state. The results show that the valence of Ni and Fe elements in NiFe-MOF is +2. Combined with the mass ratio of Ni and Fe in ICP experiments, the positively charged metal sites in MOF can be quantified. When NiFe-MOF is dispersed in aqueous solution, these metal species indeed are ligated with H_2O molecules.

Our observation opens opportunities to process MOFs for many applications, for example enabling size fractionation of sheet-like NiFe-MOF according to their lateral dimensions.^{30,31} It is known that the structural features of MOFs have a great influence on its properties including lateral size, thickness, crystal plane etc.³² In general, small-size MOFs are suitable for applications involving catalysis,⁷ biosensing⁵ and gas separation,⁹ while large-size MOFs may restack themselves to form three-dimensional stereo-structure for gas and energy storage.^{3,11} Therefore, it is important to control the sizes of MOFs toward specific applications.³² However, it remains significant challenge to process MOFs for size fractionation in solid states. This is because of MOFs' large specific surface areas, where the particles tend to aggregate in dehydration state through van der Waals interactions.^{34,35}

Consequently, the development of synthetic strategies that could facilitate MOF processability in the liquid phase is desirable. In the present study, the above negatively charged NiFe-MOF aqueous dispersion was further disposed by size fractionation to separate NiFe-MOF with different sizes.³⁷ As shown in Figures 4A and 4F, the zeta potentials of NiFe-MOF dispersions can be modified by titrating in a small amount of hydrochloric acid (HCl), leading to the precipitation of nanosheets after standing still overnight. The supernatant suspension and sediment were independently collected and denoted as small-size- (S-MOF; zeta potential of +29.5 mV) and large-size-MOF (L-MOF, zeta potential of +16.9 mV, inset of Figure 4A), respectively. Despite of both samples' characteristics of ultrathin and almost transparent lamellar structures, the lateral size of S-MOF is in the range of 40–80 nm and L-MOF of 120–200 nm (Figures 4B–4E). Several further characterization experiments (XPS, UV-vis and FT-IR, Figures 3C–3F, 4G, 4H, and S7–S16) reveals that both S- and L-MOFs contain Ni, Fe, O, and C as the main components with similar features as the pristine NiFe-MOF.^{27,29}

In a typical linear sweep voltammogram (LSV) plot (Figure 4I), the cathodic current of S-MOF increases as the potential becomes more negative, signifying a typical oxygen evolution process. As comparison to L-MOF counterpart, the S-MOF electrode exhibits significantly enhanced OER actives as evidenced by its small Tafel slopes (49 vs. 61 mV dec^{-1} for L-MOF), smaller charge-transfer resistance (EIS spectra in

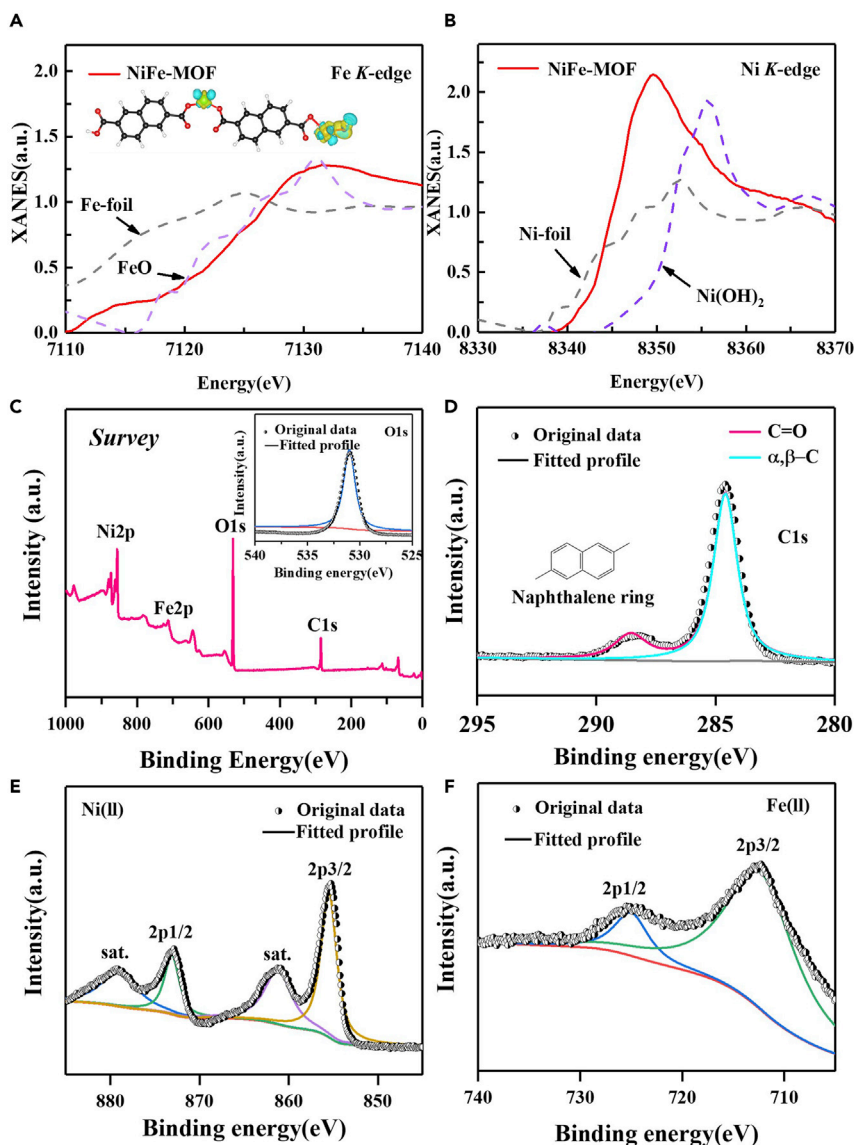


Figure 3. Structure characterization of NiFe-MOF

(A) The Fe K-edge XANES spectra for NiFe-MOF as comparison to FeO and Fe-foil counterparts.

(B) The Ni K-edge XANES spectra for NiFe-MOF as comparison to Ni(OH)₂ and Ni-foil.

(C–F) XPS survey, C_{1s}, O_{1s}, Ni_{2p} and Fe_{2p} spectra of NiFe-MOF. Next, S-MOF was then applied for the electrocatalytic oxygen evolution reaction (OER) in 1 M KOH electrolyte in a typical three-electrode system. The working electrode has been prepared by depositing S-MOF onto nickel foam (NF) substrate with an optimal mass loading of ~2.5 mg cm⁻² (Figure S17–S20). All the data were acquired without *iR*-correction.

Figure S21). This result is consistent to the results from electrochemically active surface areas (ECSA), where S-MOF electrode is 4.8 times of L-MOF (15.22 vs. 3.13 mF cm⁻², Figure S22). In addition, the properties of commercial IrO₂ were tested under the same conditions, whose overpotential is 446 mV at 10 mA cm⁻² and ECSA is 5.6 mF, and thus are far lower than those of S-MOF. Furthermore, the S-MOF electrode has shown excellent catalytic stability with minor activity decay after operation for 30 h in a chronoamperometric test (Figures 4K and S23, showing the characteristic peak of the organic ligand still exists after stability test).^{32,37}

It can be seen from XPS (Figures 3C, S7, and S12) that the O/C ratio in the obtained S-MOF is significantly reduced. Consequently, as comparison to L-MOF, the carboxyl content in S-MOF is reduced, and more metal nodes that do not fully coordinate with organic ligands are exposed. This result is consistent to

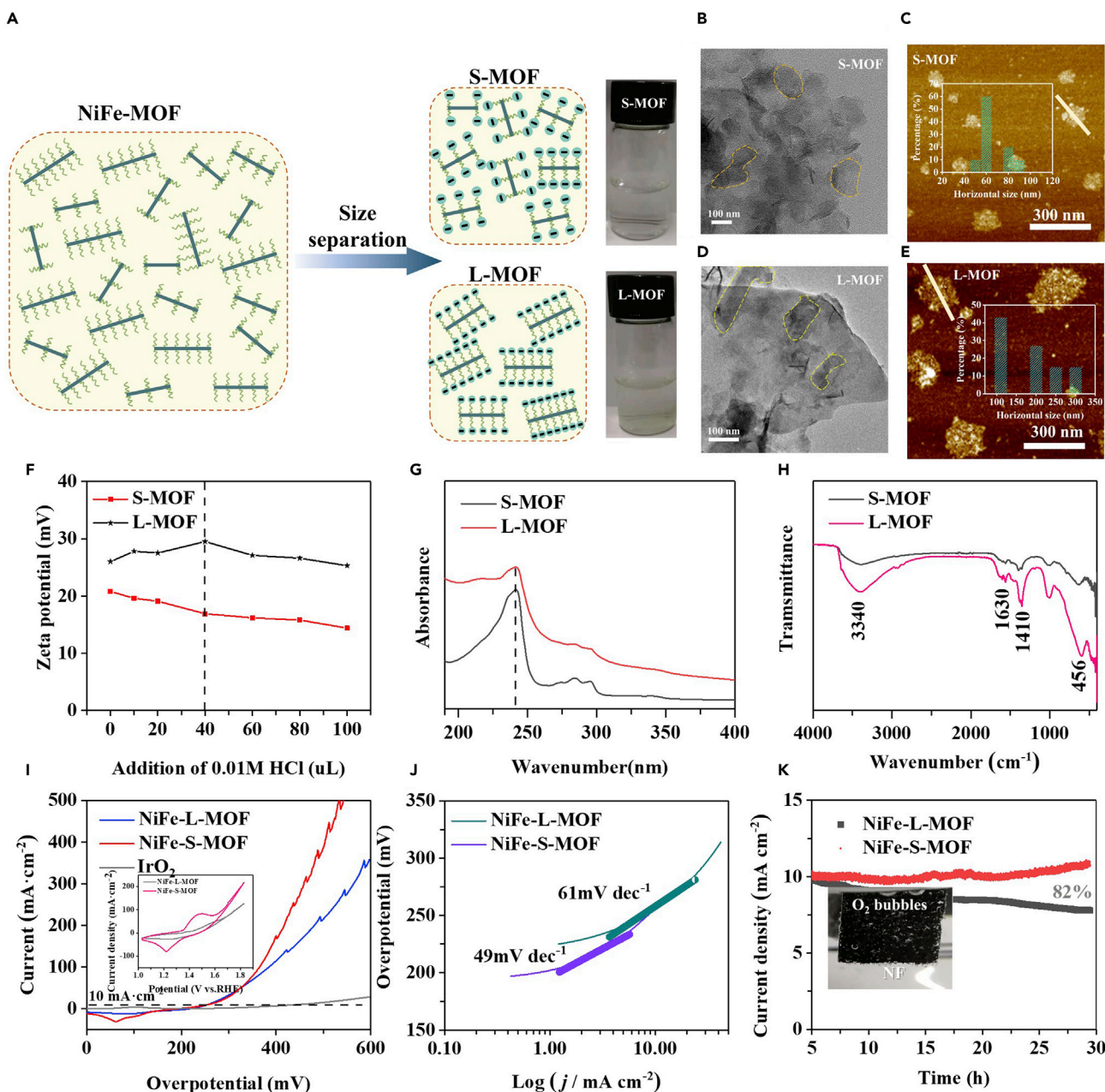


Figure 4. Applications of NiFe-MOF aqueous dispersions for size fractionation according to their lateral dimensions (S- and L-MOF) and their electrocatalytic properties for oxygen evolution reaction (OER)

(A) Schematic illustration of the size fractionation of NiFe-MOF. The right are photographs of S-MOF (up) and L-MOF (down) aqueous solutions. (B and D) High-resolution transmission electron microscopy (HRTEM) images of S- and L-MOF. (C and E) Atomic force microscopy (AFM) images of S- and L-MOF with the size distribution histograms. (F) Zeta potential of S- and L-MOF dispersions (1 mg mL⁻¹ original NiFe-MOF nanolayer aqueous, 5 mL) as a function of the added amount of 0.01M of HCl solution (0, 20, 40, 60, 80, 100 μ L). (G) UV-vis spectra of S- and L-MOF aqueous solutions. (H) FTIR spectra of S- and L-MOF, showing that both contain four main absorption bands at 3340, 1630, 1410 and 456 cm⁻¹. (I) Linear scan voltammogram (LSV) plots obtained with S-MOF, L-MOF and IrO₂ for OER at 10 mV s⁻¹ in 1 M KOH; The insert are CV plots of S- and L-MOF. (J) Tafel plots of S- and L-MOF. (K) Chronoamperometric testing of S- and L-MOF for 15,000 s at current density of 10 mA cm⁻² (vs. RHE) in 1 M KOH; The inset photograph shows the evolution of oxygen gas bubbles at the S-MOF electrode at an applied cell voltage of 1.6 V.

CV test (illustration of Figure 4I), where there is an obvious redox peak in the S-MOF as comparison to L-MOF, indicating that the metal sites in the S-MOF are more likely to be activated into the active state. Further, XRD test (Figure S2) shows that the obtained S-MOF and L-MOF are consistent, however the lateral size of S-MOF is smaller than L-MOF in AFM images, leading to more edge exposure, which may be the reason why S-MOF has good OER performance.

As an excellent OER material, S-MOF was also used as the cathode material for Zn-air battery. The primary fuel cell formed with zinc flakes as cathode material to electrically drive small bulbs. After charging for 10 min at a current density of 10 mA cm^{-2} , it can provide 1.97 V voltage and drive small bulbs to emit light.

DISCUSSION

In summary, we have conducted a systematic study combining theoretical models and experiments for synthesizing “clean” MOF aqueous dispersions. The additive-free feature allows for further fabrication of MOFs-based hybrid architectures with many other functional materials. The ease of preparation and the remarkable aqueous processability of MOFs make this emerging nanostructure promising not only for traditional technological fields such as catalysis, but also emerging areas such as membranes, nitrogen electroreduction, water splitting and catalysis s. It is believed that the present work has promoted a significant step forward to bringing MOFs closer to commercialization.

Limitations of the study

We believe that the design of the present work takes an important step toward commercialization of MOFs. However, this study only analyzed two-dimensional MOF, and there was a lack of studies on more different types of others microstructures.

STAR★METHODS

Detailed methods are provided in the online version of this paper and include the following:

- KEY RESOURCES TABLE
- RESOURCE AVAILABILITY
 - Lead contact
 - Materials availability
 - Data and code availability
- METHOD DETAILS
 - Synthesis of NiFe-MOF dispersions
 - Size fractionation of NiFe-MOF nanosheets
 - Working electrode preparation based on S-MOF for electrocatalytic oxygen evolution reactions (OER)
 - Physical characterizations
 - Electrochemical characterizations
 - Zn-air battery driven small bulb based on S-MOF cathode material
 - Computational methods

SUPPLEMENTAL INFORMATION

Supplemental information can be found online at <https://doi.org/10.1016/j.isci.2023.106239>.

ACKNOWLEDGMENTS

The authors would like to acknowledge the financial and equipment supports from National Natural Science Foundation of China (Grant No. 92163124, 51888103 and 52006105), Australian Research Council (FT210100364), Jiangsu Natural Science Foundation (Grant No. BK20190460), Fundamental Research Funds for the Central Universities (Grant No. 30920041113 and 30921013103) and BL14W1 beamline at the Shanghai Synchrotron Radiation Facility.

AUTHOR CONTRIBUTIONS

S.C. conceived the idea and coordinated the study and led writing of the manuscript; L.C.Y. and Z.H.N. contributed to microscopy characterization and analysis; S.C.X., L.L.J., B.K.X. and M.L. contributed to

electrochemical test and analysis and rest physical characterizations and analysis. All co-authors discussed the results and made comments on the manuscript.

DECLARATION OF INTERESTS

The authors declare that they have no known competing financial interests or personal relationships that could have appeared to influence the work reported in this paper.

INCLUSION AND DIVERSITY

We worked to ensure sex balance in the selection of non-human subjects.

We worked to ensure diversity in experimental samples through the selection of the cell lines.

While citing references scientifically relevant for this work, we also actively worked to promote gender balance in our reference list.

We avoided “helicopter science” practices by including the participating local contributors from the region where we conducted the research as authors on the paper.

Received: October 28, 2022

Revised: January 30, 2023

Accepted: February 15, 2023

Published: February 18, 2023

REFERENCES

- Perinot, A., Passarella, B., Giorgio, M., and Caironi, M. (2020). Walking the route to ghz solution-processed organic electronics: a heroic exploration. *Adv. Funct. Mater.* **30**, 1907641.
- Feng, S., Shang, Y., Wang, Z., Kang, Z., Wang, R., Jiang, J., Fan, L., Fan, W., Liu, Z., Kong, G., et al. (2020). Fabrication of a hydrogen-bonded organic framework membrane through solution processing for pressure-regulated gas separation. *Angew. Chem. Int. Ed. Engl.* **59**, 3840–3845.
- Ding, L.P., Mclean, B., Xu, Z., Kong, X., Hedman, D., Qiu, L., Page, A.J., and Ding, F. (2022). Why carbon nanotubes grow. *J. Am. Chem. Soc.* **144**, 5606–5613.
- Ackermann, J., Metternich, J.T., Herbertz, S., and Kruss, S. (2022). Biosensing with fluorescent carbon nanotubes. *Angew. Chem. Int. Ed. Engl.* **61**, e202112372.
- Heikkilä, T.T. (2022). Surprising superconductivity of graphene. *Science* **375**, 719–720.
- Deng, H., Grunder, S., Cordova, K.E., Valente, C., Furukawa, H., Hmadeh, M., Gándara, F., Whalley, A.C., Liu, Z., Asahina, S., et al. (2012). Large-pore apertures in a series of metal-organic frameworks. *Science* **336**, 1018–1023.
- Liao, P.Q., Shen, J.Q., and Zhang, J.P. (2018). Metal-organic frameworks for electrocatalysis. *Coord. Chem. Rev.* **373**, 22–48.
- Liao, P.Q., Zhang, W.X., Zhang, J.P., and Chen, X.M. (2015). Efficient purification of ethene by an ethane-trapping metal-organic framework. *Nat. Commun.* **6**, 8697.
- Bao, Z., Chang, G., Xing, H., Krishna, R., Ren, Q., and Chen, B. (2016). Potential of microporous metal-organic frameworks for separation of hydrocarbon mixtures. *Energy Environ. Sci.* **9**, 3612–3641.
- Cui, X., Chen, K., Xing, H., Yang, Q., Krishna, R., Bao, Z., Wu, H., Zhou, W., Dong, X., Han, Y., et al. (2016). Pore chemistry and size control in hybrid porous materials for acetylene capture from ethylene. *Science* **353**, 141–144.
- Herm, Z.R., Wiers, B.M., Mason, J.A., van Baten, J.M., Hudson, M.R., Zajdel, P., Brown, C.M., Masciocchi, N., Krishna, R., and Long, J.R. (2013). Separation of hexane isomers in a metal-organic framework with triangular channels. *Science* **340**, 960–964.
- Liao, P.Q., Huang, N.Y., Zhang, W.X., Zhang, J.P., and Chen, X.M. (2017). Controlling guest conformation for efficient purification of butadiene. *Science* **356**, 1193–1196.
- Cai, W., Wang, J., Chu, C., Chen, W., Wu, C., and Liu, G. (2019). Metal-organic framework-based stimuli-responsive systems for drug delivery. *Adv. Sci.* **6**, 1801526.
- Sun, H., Kong, X., Park, H., Liu, F., Lee, Z., and Ding, F. (2022). Spiral growth of adlayer graphene. *Adv. Mater.* **34**, 2107587.
- Guo, S., Garaj, S., Bianco, A., and Ménard-Moyon, C. (2022). Controlling covalent chemistry on graphene oxide. *Nat. Rev. Phys.* **4**, 247–262.
- Vasylenko, A., Gamon, J., Duff, B.B., Gusev, V.V., Daniels, L.M., Zanella, M., Shin, J.F., Sharp, P.M., Morscher, A., Chen, R., et al. (2021). Element selection for crystalline inorganic solid discovery guided by unsupervised machine learning of experimentally explored chemistry. *Nat. Commun.* **12**, 5561.
- Chang, R., Wu, X., Cheung, O., and Liu, W. (2022). Synthetic solid oxide sorbents for CO₂ capture: state-of-the art and future perspectives. *J. Mater. Chem.* **10**, 1682–1705.
- Sezginel, K.B., Keskin, S., and Uzun, A. (2016). Tuning the gas separation performance of CuBTC by ionic liquid incorporation. *Langmuir* **32**, 1139–1147.
- Knebel, A., Bavykina, A., Datta, S.J., Sundermann, L., Garzon-Tovar, L., Lebedev, Y., Durini, S., Ahmad, R., Kozlov, S.M., Shterk, G., et al. (2020). Solution processable metal-organic frameworks for mixed matrix membranes using porous liquids. *Nat. Mater.* **19**, 1346–1353.
- He, S., Chen, L., Cui, J., Yuan, B., Wang, H., Wang, F., Yu, Y., Lee, Y., and Li, T. (2019). General way to construct micro- and mesoporous metal-organic framework-based porous liquids. *J. Am. Chem. Soc.* **141**, 19708–19714.
- Li, C., Liu, J., Zhang, K., Zhang, S., Lee, Y., and Li, T. (2021). Coating the right polymer: achieving ideal metal-organic framework particle dispersibility in polymer matrixes using a coordinative crosslinking surface modification method. *Angew. Chem. Int. Ed. Engl.* **60**, 14138–14145.

22. Yuan, H., Liu, G., Qiao, Z., Li, N., Buenconsejo, P.J.S., Xi, S., Karmakar, A., Li, M., Cai, H., Pennycook, S.J., and Zhao, D. (2021). Metal-organic frameworks: solution-processable metal-organic framework nanosheets with variable functionalities. *Adv. Mater.* **33**, 2170228.
23. McNamara, N.D., Neumann, G.T., Masko, E.T., Urban, J.A., and Hicks, J.C. (2013). Catalytic performance and stability of (V) MIL-47 and (Ti) MIL-125 in the oxidative desulfurization of heterocyclic aromatic sulfur compounds. *J. Catal.* **305**, 217–226.
24. Jayaramulu, K., Masa, J., Tomanec, O., Peeters, D., Ranc, V., Schneemann, A., Zboril, R., Schuhmann, W., and Fischer, R.A. (2017). Electrocatalysis: nanoporous nitrogen-doped graphene oxide/nickel sulfide composite sheets derived from a metal-organic framework as an efficient electrocatalyst for hydrogen and oxygen evolution. *Adv. Funct. Mater.* **33**, 27.
25. Cui, G., Li, G., Luo, D., Zhang, Y., Zhao, Y., Wang, D., Wang, J., Zhang, Z., Wang, X., and Chen, Z. (2020). Three-dimensionally ordered macro-microporous metal organic frameworks with strong sulfur immobilization and catalyzation for high-performance lithium-sulfur batteries. *Nano Energy* **72**, 104685.
26. Ai, L., Zhang, C., Li, L., and Jiang, J. (2014). Iron terephthalate metal-organic framework: revealing the effective activation of hydrogen peroxide for the degradation of organic dye under visible light irradiation. *Appl. Catal. B Environ.* **148–149**, 191–200.
27. Nguyen, V., Nguyen, T., Bach, L., Hoang, T., Bui, Q., Tran, L., Nguyen, C., Vo, D.V., and Do, S. (2018). Effective photocatalytic activity of mixed Ni/Fe-base metal-organic framework under a compact fluorescent daylight lamp. *Catalysts* **8**, 487.
28. Sun, Y., Ding, S., Xu, S., Duan, J., and Chen, S. (2021). Metallic two-dimensional metal-organic framework arrays for ultrafast water splitting. *J. Power Sources* **494**, 229733.
29. Duan, J., Chen, S., and Zhao, C. (2017). Ultrathin metal-organic framework array for efficient electrocatalytic water splitting. *Nat. Commun.* **8**, 15341.
30. Wang, H., Liu, X., Niu, P., Wang, S., Shi, J., and Li, L. (2020). Porous two-dimensional materials for photocatalytic and electrocatalytic applications. *Matter* **2**, 1377–1413.
31. Niu, W., He, J., Gu, B., Liu, M., and Chueh, Y. (2021). Opportunities and challenges in precise synthesis of transition metal single-atom supported by 2D materials as catalysts toward oxygen reduction reaction. *Adv. Funct. Mater.* **31**, 2103558.
32. Zhao, C.X., Li, B.Q., Liu, J.N., and Zhang, Q. (2021). Intrinsic electrocatalytic activity regulation of M-N-C single-atom catalysts for the oxygen reduction reaction. *Angew. Chem. Int. Ed. Engl.* **60**, 4448–4463.
33. Dechnik, J., Gascon, J., Doonan, C.J., Janiak, C., and Sumbly, C.J. (2017). Mixed-matrix membranes. *Angew. Chem. Int. Ed. Engl.* **56**, 9292–9310.
34. Seoane, B., Coronas, J., Gascon, I., Etxeberria Benavides, M., Karvan, O., Caro, J., Kapteijn, F., and Gascon, J. (2015). Metal-organic framework based mixed matrix membranes: a solution for highly efficient CO₂ capture? *Chem. Soc. Rev.* **44**, 2421–2454.
35. Cheng, W., Zhao, X., Su, H., Tang, F., Che, W., Zhang, H., and Liu, Q. (2019). Lattice-strained metal-organic-framework arrays for bifunctional oxygen electrocatalysis. *Nat. Energy* **4**, 115–122.
36. Sun, Y., Jiang, T., Duan, J., Jiang, L., Hu, X., Zhao, H., Zhu, J., Chen, S., and Wang, X. (2020). Two-dimensional nanomesh arrays as bifunctional catalysts for N₂ electrolysis. *ACS Catal.* **10**, 11371–11379.
37. Li, Z., Wei, L., Jiang, W.J., Hu, Z., Luo, H., Zhao, W., Xu, T., Wu, W., Wu, M., and Hu, J.S. (2019). Chemical state of surrounding iron species affects the activity of Fe-N_x for electrocatalytic oxygen reduction. *Appl. Catal. B Environ.* **251**, 240–246.
38. Nguyen, A.N., Tran, N.M., and Yoo, H. (2022). Direct growth and post-treatment of zeolitic imidazolate framework-67 on carbon paper: an effective and stable electrode system for electrocatalytic reactions. *J. Mater. Chem.* **10**, 20770–20778.
39. Li, H., Luo, X., Chen, M., Liu, C., Wu, X., Feng, Y., and Zhang, B. (2022). Porous organic polymers involving chloro-substituted peryleneimide for photocatalytic water oxidation under visible light irradiation. *Chem. Eng. J.* **443**, 136463.
40. Bockris, J.O., and Otagawa, T. (1984). The electrocatalysis of oxygen evolution on perovskites. *J. Electrochem. Soc.* **131**, 290–302.
41. Song, F., and Hu, X. (2014). Exfoliation of layered double hydroxides for enhanced oxygen evolution catalysis. *Nat. Commun.* **5**, 4477.
42. Wang, Y., Qiao, M., Li, Y., and Wang, S. (2018). Tuning surface electronic configuration of nife ldhs nanosheets by introducing cation vacancies (Fe or Ni) as highly efficient electrocatalysts for oxygen evolution reaction. *Small* **14**, 1800136.

STAR★METHODS

KEY RESOURCES TABLE

REAGENT or RESOURCE	SOURCE	IDENTIFIER
Chemicals, peptides, and recombinant proteins		
Nickel acetate ($\text{Ni}(\text{Ac})_2 \cdot 4\text{H}_2\text{O}$, 98%)	Sigma-Aldrich	6018-89-9
Iron nitrate ($\text{Fe}(\text{NO}_3)_3 \cdot 9\text{H}_2\text{O}$, 98%)	Sigma-Aldrich	7782-61-8
2,6-Naphthalenedicarboxylic acid dipotassium	Sigma-Aldrich	2666-06-0
Potassium hydroxide (KOH, 99%)	Sigma-Aldrich	1310-58-3
Hydrochloric acid (HCl, 36%)	Sigma-Aldrich	7647-01-0
Nafion solution (5 wt%)	Sigma-Aldrich	31175-20-9
Deposited data		
PowerPoint 2019	Microsoft	www.microsoftstore.com.cn
Software and algorithms		
MedeA-VASP	Materials Design, Inc.	https://www.materialsdesign.com/
Other		
Thermo Scientific ICAP 6500 duo optical emission spectrometer	Thermo	https://www.thermofisher.cn/
SHIMADZU UV-2600 spectrophotometer	SHIMADZU	https://www.shimadzu.com/
Tecnaï G2 Spirit and JEOL JEM-ARM200F	Japan Electronics Co., Ltd	https://www.jeol.co.jp/

RESOURCE AVAILABILITY

Lead contact

Further information and requests for resources should be directed to and will be fulfilled by the lead contact, Sheng Chen (sheng.chen@njust.edu.cn).

Materials availability

The materials that support the findings of this study are available from the corresponding authors upon reasonable request. This study did not generate new unique reagents.

Data and code availability

- Data reported in this paper will be shared by the [lead contact](#) upon request.
- DFT calculation model and data are available from the [lead contact](#) upon request.
- Any additional data supporting findings on this study are available from the [lead contact](#) upon request.

METHOD DETAILS

Synthesis of NiFe-MOF dispersions

In a typical synthesis procedure, a mixed solution was made of 10 mL of DI-water, 80 mg of $\text{Ni}(\text{Ac})_2 \cdot 4\text{H}_2\text{O}$ and 20 mg of $\text{Fe}(\text{NO}_3)_3 \cdot 9\text{H}_2\text{O}$. Next, 100 mg of organic ligand 2,6-naphthalenedicarboxylate tetrahydrate was added into the above solution, and the vial was sealed for reaction at 60°C for 20 h. After cool down to room temperature, the product was collected and dialyzed for 24 h, and then redispersed in DI-water to form a colloidal suspension ($\sim 0.2 \text{ mg mL}^{-1}$).

Size fractionation of NiFe-MOF nanosheets

The zeta potential of NiFe-MOF nanosheets aqueous dispersions (0.2 mg mL^{-1}) was adjusted by 0.01 M HCl and the processed solutions were left to stand overnight. During this process, part of the NiFe-MOF

was precipitated. Both the sediment and the residual dispersions were collected and dialyzed with DI-water respectively. These two NiFe-MOF fractions are defined as L-MOF and S-MOF.

Working electrode preparation based on S-MOF for electrocatalytic oxygen evolution reactions (OER)

1 mg of S-MOF, 1 mg of acetylene black, 30 μL of Nafion solution (5 wt%) were dispersed in 750 μL of isopropanol and 220 μL of water by ultrasonication for 1 h to form a homogeneous ink. Then, the dispersion was evenly dropped on the hydrophobic carbon paper with area of 1.0 cm^{-2} and loading level from 0.2 mg cm^{-2} to 3.0 mg cm^{-2} , followed by dry under ambient conditions. L-MOF and pristine NiFe-MOF were also prepared as working electrodes according to the preparation process of S-MOF.

Physical characterizations

XRD was performed on a Philips 1130 X-ray diffractometer (40 kV, 25 mA, Cu K α radiation, $\lambda = 1.5418\text{ \AA}$); XPS was performed on an Axis Ultra (Kratos Analytical, UK) XPS spectrometer equipped with an Al K α source (1486.6 eV); inductively coupled plasma optical emission spectrometer (ICP-OES) methodology was used for elemental analysis conducted on a Thermo Scientific ICAP 6500 duo optical emission spectrometer fitted with a simultaneous charge induction detector; FT-IR spectra were recorded on a Nicolet 6700 spectrometer; UV-vis spectra were performed on a SHIMADZU UV-2600 spectrophotometer; Zeta potential was monitored on a Malvern ZS90 Zetasizer Nano series analyzer; AFM was conducted on Bruker Dimension ICON SPM using peak force mode; morphologies of the samples were observed on TEM (Tecnai G2 Spirit and JEOL JEM-ARM200F) and SEM (QUANTA 450); X-ray absorption near-edge structure (XANES) spectra were carried out at the BL14W1 beamline at the Shanghai Synchrotron Radiation Facility. For comparison, a series of spectra standards (Fe foil, FeO, Ni foil and Ni(OH) $_2$) were also collected.

Electrochemical characterizations

OER was studied in a standard three-electrode glass cell connected to a 760E workstation (Pine Research Instruments, US) using the NiFe-MOF as the working electrode, carbon rod as a counter electrode, and Hg/ HgO/ KOH (1 M) as a reference electrode. All the measured potentials were converted to reversible hydrogen electrodes (RHE) according to Potential = $E_{\text{Hg/HgO}} + 0.059\text{ pH} + 0.098$. The electrolyte was prepared using DI-water ($18.25\text{ M}\Omega\text{ cm}^{-1}$) and KOH. LSV and CV plots were recorded with the scan rates of 5 mV s^{-1} and 10 mV s^{-1} , respectively; Tafel plots were recorded with the linear portions at low overpotential fitted to the Tafel equation ($\eta = b \log j + a$, where η is overpotential, j is the current density, and b is the Tafel slope); EIS was recorded under the following conditions: AC voltage amplitude 0 or 1.5V, frequency ranges 106 to 0.01 Hz, and open circuit; the current density was normalized to the geometrical area; All CV and LSV data was presented without iR correction.

The electrochemical specific surface areas (ECSAs) of MOF nanosheets electrodes were measured by cyclic voltammetry (CV) in the potential window of 1.228–1.328 V (vs. RHE) with different scan rates of 110, 130, 150, 170 and 190 mV s^{-1} in 1 M KOH electrolyte. The plot of ΔJ ($J_a - J_c$, mA) at 1.25 V (vs. RHE) against the scan rate was nearly linear, and its slope is twice the double layer capacitance (C_{dl} , mF). We then used the benchmark specific capacitance of $C_s = 0.035\text{ mF cm}^{-2}$ to estimate the ECSAs of various electrodes ($\text{ECSA} = C_{dl}/C_s$). The S-MOF and L-MOF electrode durability were tested by chronoamperometric response which was conducted at a potential (vs. Hg/HgO) corresponding to certain current density (10 mA cm^{-2}) for 20 h.

Zn-air battery driven small bulb based on S-MOF cathode material

5 mg of S-MOF and 30 μL of Nafion solution (5 wt%) were dispersed in 750 μL of isopropanol and 220 μL of water by ultrasonication for 1 h to form a homogeneous ink. Then, the dispersion was evenly dropped onto the nickel foam with an area of 2.0 cm^{-2} , followed by dry under ambient condition. We use Zn sheet as the cathode material, 3M KOH+0.5M zinc acetate mixed solution as the electrolyte, and CHI 760 workstation to charge the electrolytic cell for 10 min at a current density of 10 mA cm^{-2} , and finally light up the small bulb.

Computational methods

First-principles calculations are performed using the Mede A-VASP based on DFT within the planewave basis set approach. The electron-ion interactions are described by the Density function method, and the electron-electron exchange correlations are described by the Perdew-Burke-Ernzerhof (PBE) functional.

For the structure optimization, we use the RMM-DIIS update algorithm. We use low precision for efficient computation and normal precision for accurate computation. The convergence is 0.08 and 0.05 for efficiency and accuracy computation. Both efficiency and accuracy computation use 400 eV planewave cutoff. A Gaussian smearing with a width of 0.05 eV was also utilized. For the surface Brillouin zone integration, a $1 \times 1 \times 1$ Monkhorst–Pack kpoint mesh was used. The convergence criteria for electronic self-consistent iteration and ionic relaxation were set to 10^{-4} eV and 10^{-5} eV. Hubbard-U correction method (DFT + U) was carried out to improve the description of highly correlated Ni/Fe 3d orbitals with the value of U set to 4.0/6.4 eV.

To evaluate the interaction strength between an adsorbed NiFe-MOF and the H_2O , the surface energy is calculated as

$$E_{\text{ads}} = E_{\text{MOF-H}_2\text{O}} - E_{\text{MOF}} - E_{\text{H}_2\text{O}}$$

where $E_{\text{MOF-H}_2\text{O}}$ is the total energy of the H_2O adsorb on the MOF, E_{MOF} is the energy of an isolated MOF calculated in a $38 \times 9.5 \times 9$ box, and $E_{\text{H}_2\text{O}}$ is the energy of the adsorption of water. E_{ads} is the energy of adsorption.